

# Minimum-density anomaly and spatial ordering of softly repulsive particles in a narrow channel

Cite this: *Soft Matter*, 2013, 9, 9876

Santi Prestipino,<sup>\*ab</sup> Franz Saija,<sup>b</sup> Alessandro Sergi<sup>c</sup> and Paolo V. Giaquinta<sup>a</sup>

We performed an extensive numerical investigation of a system of repulsive Gaussian particles confined in a thin cylindrical pore. In this setting, the fluid phase can be cooled down to very low temperatures, thus bypassing the freezing transition. Focusing on the thermal behavior of the average number density, we find a range of pressures within which, upon cooling, the system density first approaches a maximum that is then followed by a minimum at lower temperatures. As the width of the pore is reduced, the density minimum shifts to larger pressures, in line with what happens in the same model in one dimension. As far as the system structure is concerned, a pronounced layering is observed at the wall; moreover, when the pore radius is not too small, the relative fraction of solid-like (*i.e.*, well coordinated) particles increases overall on cooling, in a somewhat larger amount when crossing the region bounded by the two density extrema. On account of this phenomenology, we surmise that the anomalous behavior of the system density stems from the smoothening of the density jump occurring at the three-dimensional freezing point. By analogy, our findings suggest that the essential driving mechanism leading to the volumetric anomaly exhibited by supercooled water confined in silica nanopores at ambient pressure is an effective soft repulsion between water molecules at short distances.

Received 4th July 2013

Accepted 14th August 2013

DOI: 10.1039/c3sm51831k

[www.rsc.org/softmatter](http://www.rsc.org/softmatter)

## 1. Introduction

Particle confinement at the nanoscale provides a convenient playground for testing and evaluating the impact of reduced dimensionality on the structure, thermodynamics, and transport properties of fluids and solids. Besides being of fundamental interest, the study of low-dimensional systems may also reveal unexpected emergent behavior that is unknown to three-dimensional (3D) systems (the extraordinary physics of carbon sheets and tubes being but one notable example). We focus here on quasi-one-dimensional confinement, and particularly on (classical) dense fluid systems, where particle mobility is still sufficiently high to permit an overall structural rearrangement in response to varying thermodynamic conditions. The systems studied in this context range from hard<sup>1–6</sup> and soft spheres<sup>7,8</sup> to water (see *e.g.* ref. 9–17). For spherical particles confined in a cylindrical pore (nanochannel), both helical and columnar densest packings have been described, depending on the pore width.<sup>6</sup> Special attention has been paid to the remnants of the bulk freezing transition; it was found that stable packings with

long-range orientational order abruptly evolve into disordered packings as the particle volume fraction is reduced, making it possible to speak of a phase-transition-like behavior even for quasi-one-dimensional systems.<sup>2,3,8</sup> As for water, freezing-point depression induced by confinement in silica nanopores or carbon nanotubes has been used to probe the properties of supercooled water experimentally, down to exceptionally low temperatures. Neutron scattering experiments<sup>9,10,14,16</sup> as well as molecular-dynamics simulations<sup>12,15</sup> have shown that water molecules, far from being homogeneously distributed inside a narrow channel, display complex spatial patterns that are heavily influenced by the degree of hydrophilicity of the pore wall. While interfacial molecules are characterized by a low mobility and a glassy structure, water is more liquid-like near the pore center, where crystallization of the molecules is frustrated by the curvature of the surrounding shells.

Following a line of research that we have been pursuing in the last few years, we have carried out a Monte Carlo (MC) simulation of the Gaussian-core model (GCM)<sup>18–20</sup> in a hollow channel of small width. This fluid has been already investigated in one dimension (1D)<sup>21</sup> and on the surface of a 3D sphere;<sup>22</sup> in both cases, strict crystallization is ruled out and the fluid phase can be cooled down to virtually zero temperature (on the sphere, at a low enough temperature the system becomes glassy on the timescale of the simulation). The same thing would happen in a cylinder, provided at least that its cross-section is sufficiently small. More specifically, upon gradually reducing the width of the channel, the fluid would undergo a crossover from a 3D-like

<sup>a</sup>Università degli Studi di Messina, Dipartimento di Fisica e di Scienze della Terra, Contrada Papardo, I-98166 Messina, Italy. E-mail: [sprestipino@unime.it](mailto:sprestipino@unime.it); [paolo.giaquinta@unime.it](mailto:paolo.giaquinta@unime.it)

<sup>b</sup>CNR-IPCF, Viale F. Stagno d'Alcontres 37, I-98158 Messina, Italy. E-mail: [saija@ipcf.cnr.it](mailto:saija@ipcf.cnr.it)

<sup>c</sup>School of Chemistry and Physics, University of KwaZulu-Natal, Pietermaritzburg, and National Institute for Theoretical Physics (NITheP), KwaZulu-Natal, South Africa. E-mail: [sergi@ukzn.ac.za](mailto:sergi@ukzn.ac.za)

to a 1D-like behavior, accompanied by the suppression of the freezing transition. Near the 1D limit, we expect a whole spectrum of water-like anomalies:<sup>21</sup> in particular, in a certain range of pressures, the number density should likely exhibit, in addition to a local maximum, also a point of minimum at lower temperatures. This behavior is reminiscent of that of supercooled water in silica nanopores.<sup>9,10,16</sup>

Waterlike anomalies have been well described for effective potentials characterized by two repulsive length scales which mimic the competition between two distinct local arrangements of particles, *i.e.*, a loosely-packed (ice-type) and a more compact (water-type) arrangement. In addition to the density anomaly (*i.e.*, system expansion upon isobaric cooling), one typically observes an increase in the particle diffusivity as well as a decrease in the structural order (as measured by the two-body entropy) upon isothermal compression (see *e.g.* ref. 23–25). In some cases, including the GCM case, these anomalies occur as a cascade, with the  $(\rho, T)$  region of structural anomaly encompassing those of diffusivity and density.<sup>26,27</sup> It is a recent discovery that two repulsive scales are by no means a necessary requirement for observing waterlike anomalies with isotropic unbounded potentials,<sup>28–30</sup> in that it is sufficient that one length scale becomes more loosely defined over a range of pressures. Similarly, the GCM exhibits an anomalous melting with just one single characteristic length  $\sigma$  (the other one related to the inner core being, in a sense, zero). For low values of temperature and pressure,  $\sigma$  sets the scale of the solid lattice structure; upon compression, this length scale becomes increasingly penetrated until the crystalline order has been washed out. Hence, either a weakly softened potential with a single length scale or the GCM itself provide minimal models for investigating waterlike anomalies.

Choosing an inert cylinder so as to distil the essence of the phenomenon, we have computed the average number density of the GCM fluid upon cooling, and found a water-like minimum-density anomaly. Apparently, this feature originates from the smoothening of the density step occurring at the 3D freezing point. Accordingly, the density minimum observed in water would not be a peculiar consequence of the loose hydrogen-bond network existing in this anomalous liquid, save in the sense that this network ultimately induces a softening of the effective repulsion between pairs of molecules. Actually, the observation of a density minimum for the GCM in 1D, as well as in 2D on a sphere, suggests an additional explanation, which is more plausible for the thinnest channels, according to which the minimum-density anomaly would be a hidden feature of the supercooled GCM fluid that becomes manifest whenever permitted by the embedding geometry. This explanation is corroborated by the results of a mean-field theory for confined waterlike fluids which, while not knowing about the possibility of freezing transitions, predicts similar trends for the density maxima and minima, including pressure dependencies.<sup>31</sup>

The paper is organized as follows. We first describe the model and the simulation method in Section II, paying due attention to the way the system pressure and chemical potential are computed in a pore geometry. Our results are then presented and discussed in Section III, devoted to thermodynamic and structural properties. In particular, Section III.II presents a detailed analysis of the

radial profile of the number density as a function of temperature, for fixed values of the cylinder radius and of the imposed pressure, as well as some remarks about the typical size and distribution of patches of solid-like particles within the cylinder. Finally, we state our conclusions in Section IV.

## II. Model and method

The fluid under investigation is a system of  $N$  particles interacting *via* a bounded repulsive isotropic potential of Gaussian shape,  $v(r) = \varepsilon \exp\{-r^2/\sigma^2\}$ , where  $\varepsilon$  and  $\sigma$  are arbitrary energy and length units (from now on, the values of all quantities will be given in these units), respectively. This system provides a model for the effective pair interaction between polymers in a solution.<sup>32</sup> A distinctive feature of the GCM is reentrant melting, *i.e.*, the reappearance of the fluid phase upon isothermal compression of the solid below  $T_m \approx 0.01$ .<sup>19,20,33</sup> This entails a decreasing solid–fluid coexistence locus,  $T_m(P)$ , above the pressure  $P_M$  of the maximum melting temperature ( $P_M \approx 0.136$  in 3D (ref. 34)). A decreasing  $T_m(P)$  function is also found in water, starting with the triple-point pressure and all the way up to  $P \approx 200$  MPa.

In the present study, the particles are confined within a cylindrical box of radius  $R$  and length  $L$ , with periodic conditions along the axial  $z$  direction. The value of  $R$  was taken in the range between 1.5 and 10, and  $N$  was chosen accordingly in order that  $L$  be at least 5 times larger than  $R$  at the relevant densities, so as to avoid spurious edge effects ( $N$  ranged between 300 and 3000). No quenched molecular structure is assumed for the lateral wall, which is smooth and hard, *i.e.*, infinitely repulsive.

The simulation setup recalls the more customary isothermal–isobaric ensemble, except for the complication caused by the use of different updating rules for coordinates parallel and perpendicular to the cylinder axis. This is due to the choice of keeping  $R$  fixed while allowing  $L$  to fluctuate as a result of the imposition of a constant pressure  $P_L$  along  $z$  (for the reader's convenience, we have reported in the paper's Appendix the thermodynamic formalism appropriate to a system of particles enclosed in a long box of cylindrical shape, with a few remarks on the way the most important properties of the system are computed in the simulation). The temperature was reduced in steps  $\Delta T = 0.0005$ , starting from 0.015 and ending with 0.001 for every  $P_L$  (the values chosen for  $P_L$  were 0.3, 0.4, ..., 0.9). For  $R = 2$  and 5, we generated as many as five million MC sweeps (one sweep consisting of  $N + 1$  elementary MC moves) during the production stage of the run at temperature  $T$ , whereas an equal number of sweeps was discarded in order to allow for system relaxation to equilibrium starting from the last configuration produced at  $T + \Delta T$ . With the only exception of  $P_L = 0.4$ , the cumulated statistics was lower for other values of the radius, but still sufficiently accurate to capture at least the trends of the various properties as a function of temperature and pressure. We monitored the average number density  $n = N/(A(L))$  (with  $A = 4\pi R^2$ ), the average total energy  $E/N$ , the lateral pressure  $P_A$  (see the Appendix), and a few response functions that are also quoted in the Appendix. Moreover, we computed the radial profile  $n_1(\rho)$  ( $\rho$  measuring the distance from the axis) of the one-body density function and, for every

thin cylindrical shell, the average percentage of solid-like particles in that shell (see more below; both these functions were typically updated every 100 sweeps). Once  $n_1(\rho)$  is known, the average number  $\bar{N}(d)$  of particles that are found within a distance  $d$  from the axis is simply

$$\bar{N}(d) = 2\pi\langle L \rangle \int_0^d \rho n_1(\rho) d\rho, \quad (2.1)$$

assuming homogeneity along  $z$ , which is correct for  $\langle L \rangle \gg R$ . Obviously,  $\bar{N}(R) = N$ , which was used to check the exactness of the calculation.

Now, it is worth spending a few words to explain how, given the positions of all the system particles, we state a certain particle  $i$  to be solid-like in the given configuration. Classifying the particles as either solid-like or liquid-like is instrumental in gaining a better knowledge of the building up of spatial order on cooling, as well as to locate the crystalline patches in the pore and the preferential sites for defects. In order to decide whether the environment of particle  $i$  is more solid-like or liquid-like, we closely follow the by now standard prescription proposed by ten Wolde and coworkers,<sup>35</sup> which we recall in the following. First of all, the particles that are neighbors of  $i$  are identified: these are the  $N_b(i)$  particles  $j$  that are within a certain cutoff distance  $r_c$  from  $i$ , where  $r_c$  is taken equal to the abscissa of the first minimum of the radial distribution function (a more precise criterion to identify the neighbors, like *e.g.* the Voronoi construction, would slow down the simulation too much). Then, calling  $\hat{\mathbf{r}}_{ij}$  the unit vector specifying the orientation of the bond joining  $i$  to  $j$ , one defines a local bond-order parameter

$$\bar{q}_{lm}(i) = \frac{1}{N_b(i)} \sum_{j=1}^{N_b(i)} Y_l^m(\hat{\mathbf{r}}_{ij}), \quad (2.2)$$

$Y_l^m$  being spherical harmonics. In a crystal, at variance with what occurs in a liquid, the  $\bar{q}_{6m}(i)$  add up coherently, which is the reason why these numbers are useful to identify solid-like particles. Next, for every particle  $i$ , a normalized 13-dimensional complex vector  $\mathbf{q}_6(i)$  is defined with components proportional to  $\bar{q}_{6m}(i)$ . The dot product

$$\mathbf{q}_6(i) \cdot \mathbf{q}_6(j) = \frac{\sum_{m=-6}^6 \bar{q}_{6m}(i) \bar{q}_{6m}(j)^*}{\sqrt{\sum_{m=-6}^6 |\bar{q}_{6m}(i)|^2} \sqrt{\sum_{m=-6}^6 |\bar{q}_{6m}(j)|^2}} \quad (2.3)$$

gives a clue as to how similar the environment of  $i$  is to that of  $j$ . If  $\mathbf{q}_6(i) \cdot \mathbf{q}_6(j)$  exceeds 0.5, then particles  $i$  and  $j$  are said to be connected. If the number of particles connected to  $i$  is larger than 7, then particle  $i$  is said to be solid-like.

Finally, in order to get an insight into the spatial distribution of solid-like particles in the cylinder, we compute a function  $S(\rho)$  ("solidity") whose formal definition is

$$S(\rho) = \frac{1}{2\pi\langle L \rangle} \left\langle \sum_{i=1}^N \frac{S_i}{\rho} \delta(\rho - \rho_i) \right\rangle, \quad (2.4)$$

$S_i$  being 1 if particle  $i$  is solid-like, and 0 otherwise. In practice, for any given thin cylindrical shell, we count the average

number of solid-like particles and eventually divide this number by the shell volume.

### III. Results

#### I. Thermodynamic properties

In this section, we analyze the behavior of those thermodynamic variables – above all, the number density and the total energy – that better elucidate the characteristics of the confined GCM fluid; these properties are then contrasted with those of the 3D system. Useful indications are expected to come from the plots of the isobaric specific heat  $C_{P_L}$  and of the isothermal compressibility  $K_T$ , which show anomalous water-like behavior in both one and three dimensions.

In Fig. 1 we report the average number density  $n$  of the confined system as a function of the temperature for  $P_L = 0.4$  and for a number of  $R$  values (for later comparison, note that under a pressure of 0.4 the 3D fluid freezes into a less dense bcc crystal at  $T_m = 0.00643$  (ref. 20)). As  $R$  increases,  $n$  undergoes a crossover from a fluid-like monotonous to a non-monotonous  $T$  dependence resembling a smoothed 3D behavior. The most prominent feature seen in Fig. 1 is obviously the point of minimum which, at the considered pressure, is present for all radii except  $R = 2$ . A similar minimum is observed also in 1D and on a sphere, as well as in supercooled water confined in silica nanopores. The 3D-GCM feature that most closely resembles the density minimum is the shallow minimum present in the density of the bcc solid over the whole pressure range from 0.30 to 0.40 (see Fig. 2); below  $P = 0.30$  the average bcc density is a decreasing function of  $T$ , while it increases with  $T$  above  $P = 0.40$ .

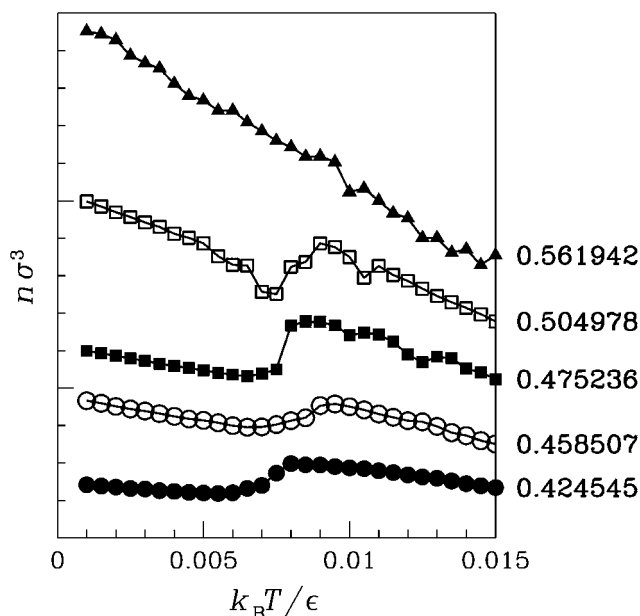


**Fig. 1** Number density  $n$  of the GCM fluid in a cylinder, plotted as a function of the temperature for  $P_L = 0.4$ . From top to bottom,  $R = 2$  ( $N = 300$ , solid triangles), 3 ( $N = 500$ , open squares), 4 ( $N = 500$ , solid squares), 5 ( $N = 800$ , open dots), and 10 ( $N = 3000$ , solid dots). Data points were vertically shifted in order to make the comparison easier. The numbers on the right are the absolute density values for  $T = 0.015$ ; the vertical scale is the same for all curves, the distance between two large ticks being 0.005.

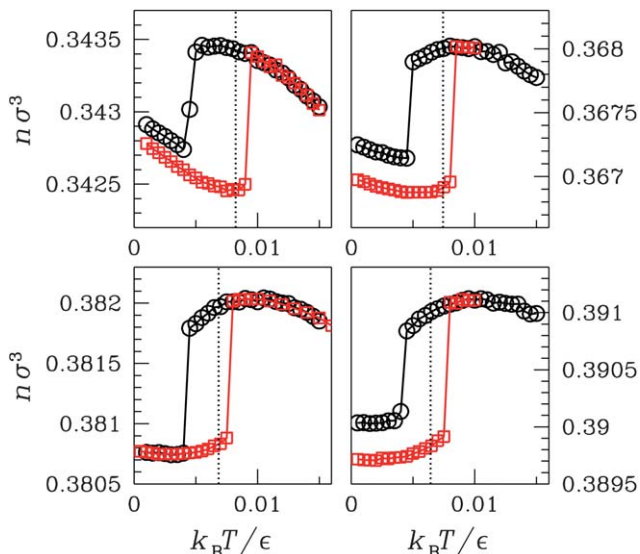


**Fig. 2** Number density  $n$  of the GCM fluid in three dimensions, plotted as a function of the temperature for a number of pressures. Left top panel:  $P = 0.30$ ; right top panel:  $P = 0.35$ ; left bottom panel:  $P = 0.38$ ; right bottom panel:  $P = 0.40$ . The liquid branch (black dots) was obtained in a cooling trajectory while the bcc-solid branch (red squares) is the result of a heating trajectory that is started at very low temperature from a perfect lattice. Each vertical dotted line marks the equilibrium freezing temperature for that pressure (as from ref. 20). It can be noted that when the liquid eventually freezes it hardly gets the right bcc density, because of residual extended crystal defects in the sample that would take much more time to be healed than our simulation time.

A second glance at Fig. 1 reveals that the small- $R$  data are affected by substantial statistical noise, indicating that the positions of the particles near the wall (*i.e.*, the vast majority for small  $R$ ) evolve more slowly than those of the particles near the axis. Actually, a more serious problem is that the low-temperature data points are rather sensitive to the system cooling rate: as we verified in a number of cases, if the cooling rate had been a factor of, say, 4 larger, then the low- $T$  branch of the density data would have had a (slightly) different slope, suggesting that the lowest- $T$  data in Fig. 1 may not be fully trustworthy. This is evidence of long system relaxation times, especially in very narrow cylinders. That said, it must be stressed that the evidence of a density minimum for  $R > 2$  is not being called into question, and should thus be considered a genuine property of the confined system.

In Fig. 3 we report the pressure behavior of  $n(T)$  for  $R = 5$ . We see from this picture that the point of minimum density is not a permanent feature of the system, *i.e.*, the density minimum only exists in a limited pressure range. Upon increasing the pressure for fixed  $R$ , the minimum is pushed to lower and lower temperatures until, beyond a certain  $P_L$  threshold, only the maximum survives. The behavior of the thermal expansion coefficient is consistent with the density evolution with pressure (data not shown). The characteristic pressure range in which a density minimum exists moves to higher pressures on reducing the radius (see the case of  $R = 2$  in Fig. 4), which is consistent with the pressure interval (between 1.2 and 1.5) where a density minimum is found in 1D.<sup>21</sup>

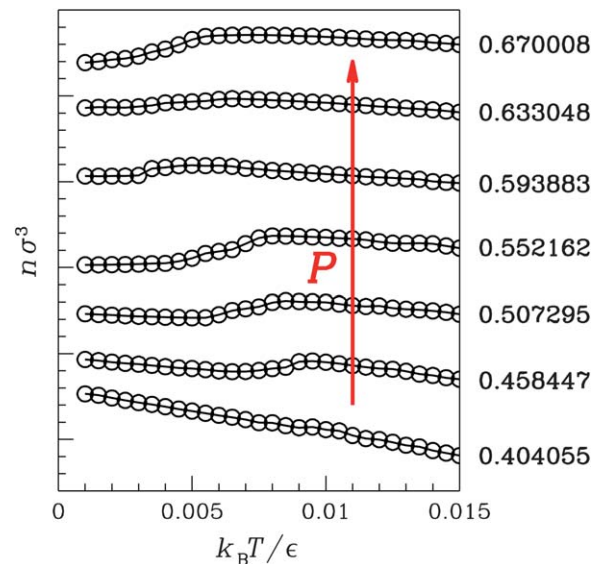


**Fig. 3** Number density  $n$  of the GCM fluid in a cylinder of radius  $R = 5$ , plotted as a function of the temperature for a number of pressures. From bottom to top,  $P_L = 0.3, 0.4, 0.5, 0.6, 0.7, 0.8, 0.9$ . Data points were vertically shifted in order to facilitate the comparison. The numbers on the right are the density values for  $T = 0.015$  (reduced units); the vertical scale is the same for all curves, the distance between two large ticks being 0.005.

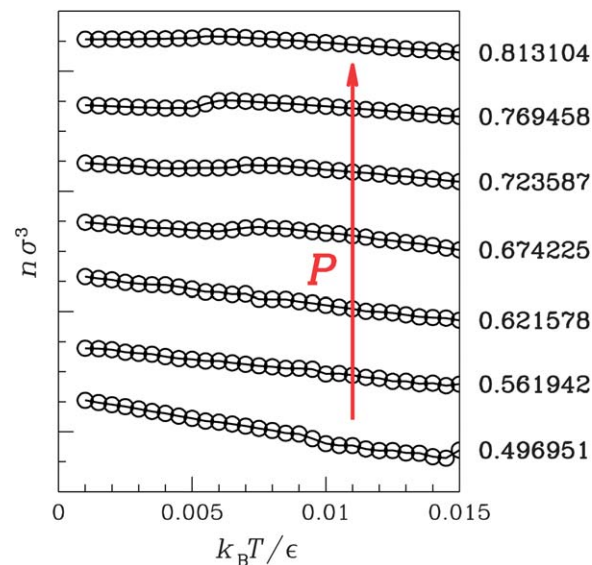


**Fig. 4** Number density  $n$  of the GCM fluid in a cylinder of radius  $R = 2$ , plotted as a function of the temperature for a number of pressures. Same notation as in Fig. 3, but the distance between two large ticks is now 0.02.

The average energy of the GCM system for  $R = 5$  is plotted as a function of temperature in the left panel of Fig. 5 for a number of  $P_L$  values. For every pressure, the energy shows a monotonic trend, with an inflection point that roughly follows the freezing-temperature locus of the 3D system. Likewise the density, also the thermal evolution of the energy is evocative of that of the 3D energy curves.

The lateral pressure  $P_A$ , defined in the Appendix, is plotted in the right panel of Fig. 5 for  $R = 5$ . At variance with  $P_L$ ,  $P_A$  is a

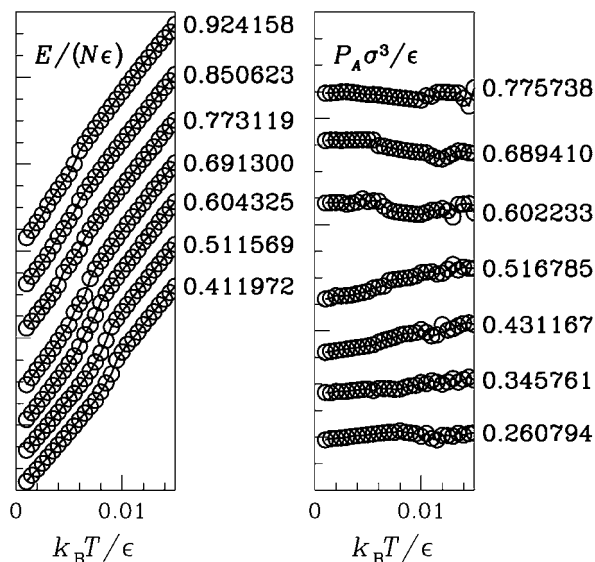


**Fig. 5** Specific total energy (left) and lateral pressure (right) of the GCM fluid in a cylinder of radius  $R = 5$ , plotted as a function of the temperature for a number of pressures. Same notation as in Fig. 3 and 4, but the distance between two large ticks is 0.02 on the left and 0.2 on the right.

fluctuating variable whose average value is only weakly dependent on  $T$ ; as a result of system anisotropy (see Section III.II),  $P_A$  is also substantially smaller than  $P_L$ . As  $R$  increases, the difference between  $P_L$  and  $P_A$  progressively reduces until it becomes negligible for  $R \gg \sigma$ .

Let us finally comment on the thermal behavior of  $C_{P_L}$  and  $K_T$  (see their definition in the Appendix) for  $R = 5$  (data not shown). Overall, the phenomenology is similar to that of the 1D and spherical-surface cases.<sup>21,22</sup> The isobaric specific heat exhibits a maximum that moves to low temperatures as the pressure increases; the  $(P_L, T)$  locus of this maximum runs very close to the isobaric minimum-expansivity line. Note that also the isobaric specific heat of water increases upon supercooling; however, in this case a  $C_p$  maximum is preempted by the occurrence of ice nucleation. Even though no experimental data are apparently available for the specific heat of supercooled water confined in silica pores, we can easily conjecture the existence of a  $C_p$  maximum also for this system at temperatures below the homogeneous-nucleation threshold (*i.e.*, below  $\approx 235$  K at ambient pressure<sup>36</sup>). As for  $K_T$ , it slightly decreases upon cooling, at a somewhat larger rate when crossing the  $T$  region where a change of concavity in the energy is observed. By the analogy with the 1D case, we expect a shallow  $K_T$  maximum to occur at larger temperatures than those sampled in our simulations.

We have also attempted to investigate the structural anomaly in a pore geometry, by first computing the radial distribution function in the axial direction only and then extracting the associated two-body entropy. The noise-to-signal ratio turned out to be large, even at high temperature ( $T = 0.015$ ); however, we easily recognize in this case the same trend as found in the 3D GCM,<sup>27</sup> with a nice  $-s_2$  maximum falling in the same pressure range where a density minimum is observed (which then shifts to higher pressures as  $R$  becomes smaller).

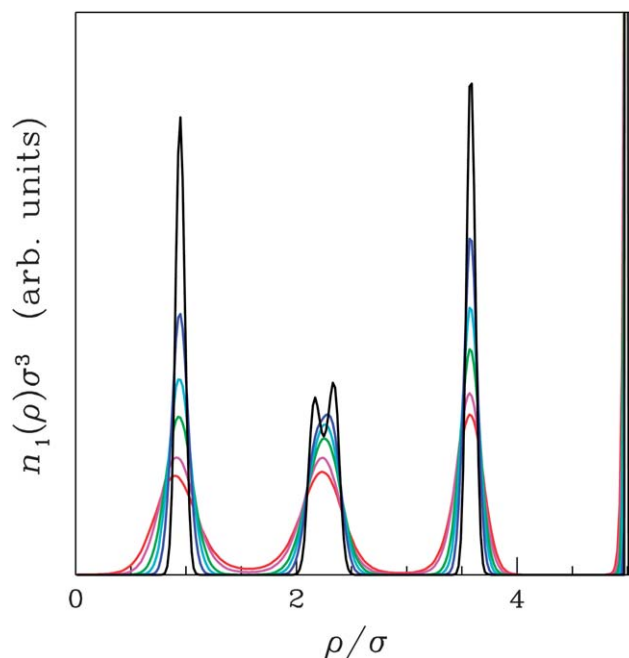


**Fig. 6** One-body density function of the GCM fluid in a cylinder of radius  $R = 5$ , plotted as a function of  $\rho$  (the distance from the axis) for  $P_L = 0.4$  and a number of temperatures  $T$ : 0.001 (black), 0.003 (blue), 0.005 (cyan), 0.007 (green), 0.009 (magenta), 0.011 (red).

## II. Structural properties

The first and most relevant effect of particle confinement in a narrow cylinder is a highly inhomogeneous density profile at low temperatures, caused by the impossibility of reconciling the natural system tendency to order as a crystal with the imposed geometric constraints. This is demonstrated for  $R = 5$  in Fig. 6, showing the radial profile of the one-body density function  $n_1(\rho)$  for  $P_L = 0.4$  and for a number of temperatures. Far from being randomly dispersed in the cylinder, the Gaussian particles are distributed in curved shells or layers around the axis (four shells for the case represented in Fig. 6), whose statistical definition becomes increasingly pronounced as the temperature is reduced. We see practically no particles located on the cylinder axis, the radius of the innermost shell being close to  $\sigma$  for the given  $R$  and  $P_L$ . For all temperatures, the sharpest shell is the outermost one, comprising particles that are in contact with the wall. Away from the wall the width of the shells is larger, indicating that inner particles move more freely than interfacial particles. Anyway, a loosely-defined shell radius might also be the consequence of thermal disorder superposed on a particle array of cubic symmetry with one axis parallel to  $z$ . It remains to see whether a sharpening of the radial definition of the shells is also accompanied by solidification, as one would guess. Since crystalline order can only be local in a cylinder, the meaning of the term “solid” here is the same as recalled in Section II, where we tagged those particles having a high number of neighbors with a local environment similar to that of the reference particle as solid-like.

For the same states whose one-body density is plotted in Fig. 6, the function  $S(\rho)$  is reported in Fig. 7. We see that solidification develops gradually on cooling, propagating from the cylinder wall

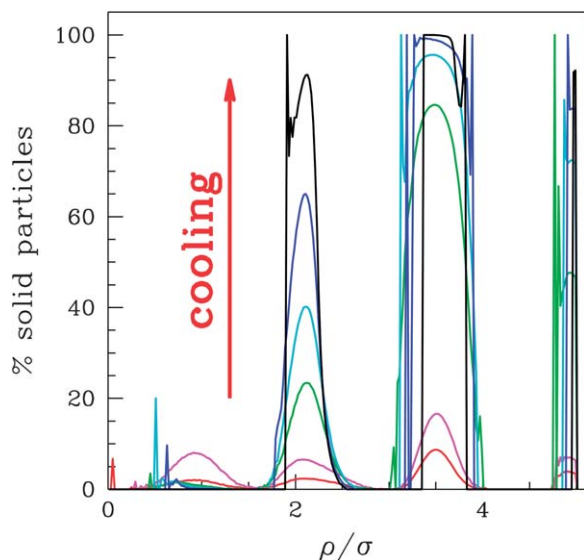


**Fig. 7** GCM fluid in a cylinder of radius  $R = 5$ : percentage of solid-like particles as a function of  $\rho$  for  $P_L = 0.4$  and the same  $T$  values as considered in Fig. 6.

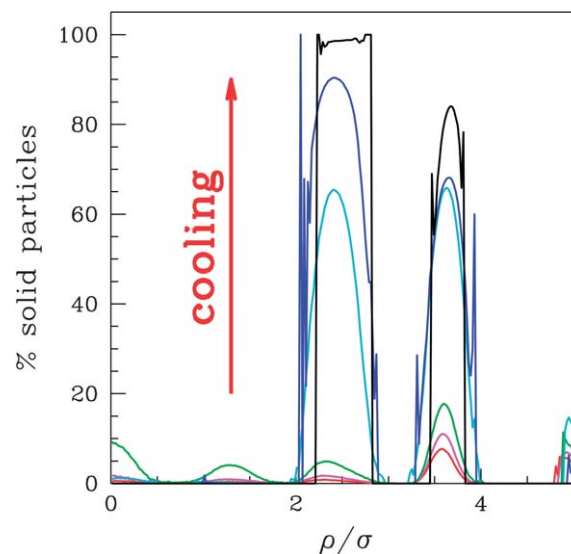


**Fig. 8** GCM fluid in a cylinder of radius  $R = 5$ : percentage of solid-like particles as a function of  $\rho$  for  $P_L = 0.8$  and the same  $T$  values as considered in Fig. 6.

to the center, and that almost all the particles in the outer shells are solid-like at the lowest temperatures. This happens even in spite of the reduced coordination of the particles at the wall, which give rise to a curved triangular layer that is admittedly well matched with the bcc-like structure of particles in the inner shells. Curiously, the more badly coordinated particles are those lying near the axis, where the highest number of mobile particles is found. By further looking at Fig. 7, we note that the number of solid-like particles in the cylinder does not grow evenly on cooling. In fact, upon moving from 0.009 to 0.007, the solid fraction undergoes a major increase which, rather interestingly, occurs in the same temperature region where the average system density drops from the maximum to the minimum value. Another example is shown in Fig. 8, which refers to  $P_L = 0.8$ . Here the number of shells is five, due to a higher system density; again, most of the solidification occurs between  $T = 0.007$  and  $T = 0.005$ , where the density loop is located. However, at variance with the lower-pressure case discussed above, particles near the wall remain fluid-like down to the lowest temperatures.

All the evidence collected so far leads us to conclude that the density minimum of the cylindrically-confined GCM fluid is the outcome of the smoothening of the 3D-freezing density step. Therefore, a sufficient condition for observing this anomaly under tube confinement would be a bulk 3D system with two properties: (i) at coexistence, the liquid should be sufficiently more dense than the solid (which requires a decreasing  $T_m(P)$  function with a large enough  $|dT_m/dP|$ ); (ii) at very low temperatures, the solid density should be a decreasing function of  $T$  over a range of pressures. It goes without saying that both conditions (i) and (ii) are fulfilled for ambient-pressure water, and the same two properties are probably generic among systems with soft pair repulsions. However, this is only part of the truth, since a minimum-density anomaly is also present in 1D. Hence, a hidden tendency to develop a density minimum is probably encoded in the Gaussian potential, as also evidenced

by the existence of a minimum in the average solid density of both 2D (ref. 21) and 3D systems (this paper).

When looking at the narrower  $R = 2$  cylinder, no analogous solidification with cooling is found, whatever the pressure. However, this just occurs because our notion of solid-like particle becomes inadequate when the cylinder is too thin. The origin of the density minimum for  $R = 2$  should have more to do with the similarity of this system with the 1D case.

A final issue is the triangular order exhibited by interfacial particles at low temperatures, which shows remarkable similarities with the structure of gold nanowires<sup>39–41</sup> and of microgel spheres inside glass capillaries.<sup>8</sup> Shown in Fig. 9 is a slice of a typical system configuration for  $R = 5$ ,  $P_L = 0.4$ , and  $T = 0.005$ , where solid-like (fluid-like) particles have been highlighted in

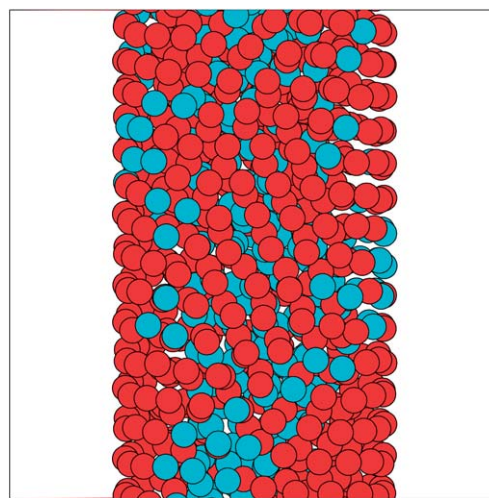


**Fig. 9** A snapshot of the GCM fluid in a cylinder of radius  $R = 5$ , for  $P_L = 0.4$  and  $T = 0.005$ : solid-like particles (red) and fluid-like particles (cyan). Only part of the system is shown in the picture.

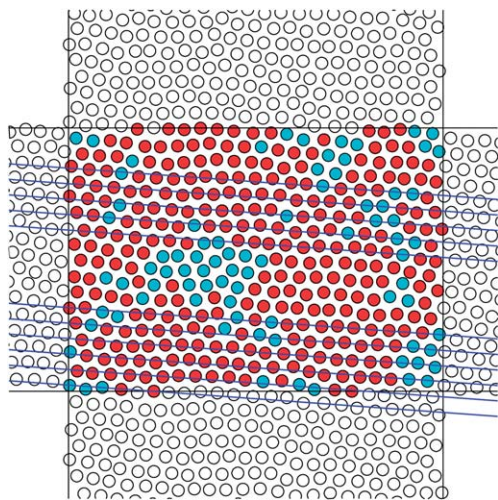


**Fig. 10** For the same configuration represented in Fig. 9, we report here a planar projection of the particles in the interfacial layer, obtained as described in the text. Solid-like particles (red) are distinguished from fluid-like particles (cyan). We also show in white the periodic images of the particles along all directions. The blue straight lines are guides to the eye, showing strands of particles along the crystallographic axis that is closer to the horizontal direction. The small non-zero slope of these lines is the evidence that the triangular array is tilted with respect to  $z$ , hence it is chiral.

red (cyan). A planar projection of the positions of the interfacial particles alone is shown in Fig. 10. This picture was constructed by first selecting out the wall particles and subsequently unfolding the cylinder onto a plane. The result is a manifestly triangular arrangement which owes its origin to the necessity of filling the interfacial layer with spheres in the most efficient way. However, owing to the requirement of a good matching with the inner particles, the triangular array is slightly tilted with respect to the vertical axis, similarly to the particle arrangements which are seen in gold nanowires freely suspended in a vacuum. However, chiral interfacial arrays are not the rule. In other conditions of radius, pressure, and temperature, more symmetric arrangements that are dual of armchair and zigzag carbon nanotubes are observed, as shown by the example illustrated in Fig. 11, which is relative to  $N = 500$ ,  $R = 1.5$ ,  $P_L = 0.5$ , and  $T = 0.005$ . It is evident from this picture that the triangular patches have a finite length, and are separated from other triangular patches of different orientation by a stripe of defects with the interfacial coordination number different from six. In the attempt to rationalize this behavior, we considered a hollow cylinder that is so thin to host only an interfacial layer and a monoatomic chain on the central axis. We reviewed arrangements of any type (see ref. 41) and particle periodicity in the chain, and for each of them we computed the  $T = 0$  chemical potential so as to eventually filter out the most stable structure for the given pressure (following a procedure similar to the one described in ref. 42). Upon increasing the pressure, we typically observe a full sequence of zero-temperature phase transitions between structures that are occasionally chiral, along with a dense crowd of other (metastable) structures that are nearly optimal, hence potentially relevant at low temperature. The lack of a net preference for a specific structure

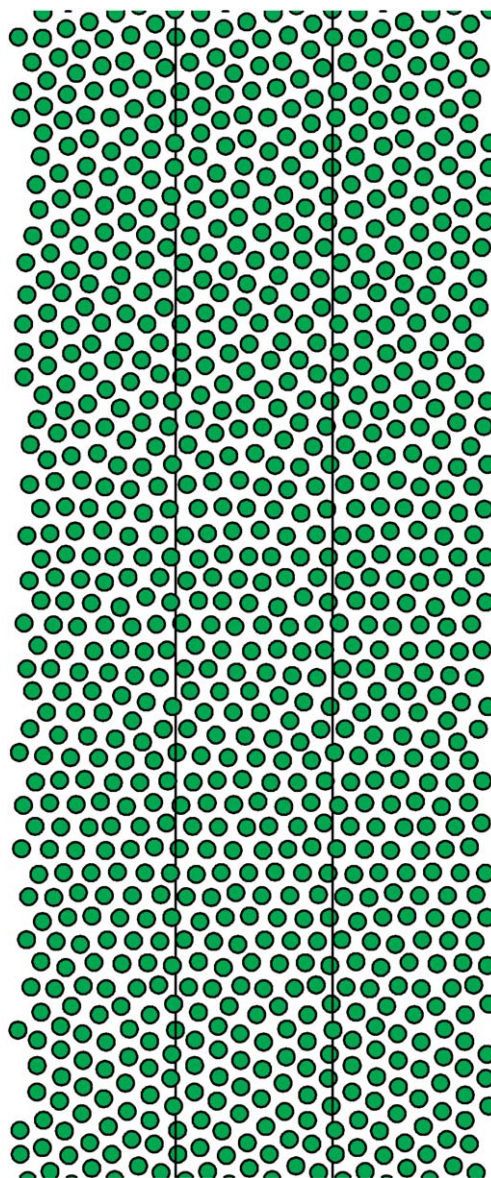


**Fig. 11** A snapshot of the GCM fluid in a cylinder of radius  $R = 1.5$ , for  $P_L = 0.5$  and  $T = 0.005$ . For this radius, there are only two shells of particles, the interfacial one and a chain running along the axis. The figure shows (only a slice of) the planar projection of the particles in the interfacial layer (green). For the sake of clarity, the system (central stripe) has been repeated periodically to the left and to the right.

is the apparent reason for the finite size of triangular patches in a small- $R$  system at low temperature. In other words, the finite size of these patches reflects the frustration characterizing the system in its search for packing optimization on cooling. This effect would be less important for  $R = 5$ , which is more bulk-dominated than  $R = 2$ , and this justifies why the properties of this system are less hampered by statistical noise.

## IV. Conclusions

In this paper, we present a numerical study of the thermodynamic and structural properties of a fluid of Gaussian particles in a long and narrow cylinder, which is meant to be a minimally

representative model for water molecules inside silica nanopores. The dimensionality of this confined fluid is intermediate between one and three dimensions. Hence, the model provides an interesting example of a geometrically-frustrated fluid which, while being unable to crystallize on cooling, can be supercooled to a large extent before becoming a glass, at least on the time scale of the simulation.

As is well known, the GCM fluid exhibits many water-like anomalies in three dimensions, including a density maximum at a temperature close to freezing (see *e.g.* ref. 43). In addition to this maximum, the cylindrically-confined system also exhibits a density minimum at lower temperatures, which however is only observed in a limited pressure interval that is shifted upwards when reducing the cylinder radius. For pressures higher than this interval, the minimum disappears and only the maximum survives, precisely as observed in the same model fluid in other confining geometries like a 1D torus or the surface of a sphere. In fact, the minimum-density anomaly is even more general since it is also observed in the solid phase of planar and 3D GCM systems. All this evidence suggests that the volumetric anomaly of GCM particles in a cylinder has a two-fold explanation: on one side, the density minimum would simply be the consequence of the smoothening of the density step occurring at 3D freezing; on the other hand, this anomaly is undoubtedly specific of the Gaussian potential, *i.e.*, of its bounded soft-core characteristic, since a density minimum is also found in the 1D space. By analogy, our findings suggest that the density minimum of nanoconfined water would have essentially the same mixed origin, and the behavior would be similar in all systems that are characterized by an effective interparticle soft repulsion.

We also looked at the uneven distribution of GCM particles inside the tube. The particles were found to be organized in layers, wrapped around the cylinder axis, which upon cooling become “solid” at different temperatures, starting from the outermost layer. We also noted that the amount of solidified matter in a not-too-narrow tube undergoes an enhancement in the temperature region of the density loop, consistently with the view that this loop is the remnant of the density jump at 3D freezing. As for the particles wetting the wall, they give rise to an extended triangular layer at low temperatures. Similarly as in gold nanowires, chiral arrangements are occasionally observed in the interfacial layer while, in other cases, arrangements of higher symmetry are found. Using zero-temperature total-energy calculations, we provide the criterion behind the selection of the surface structure in thin tubes as well as the likely reason for the finite length of the triangular surface patches at low temperature.

## Appendix

### Thermodynamics and statistical mechanics of the confined system

In this appendix we adapt the framework developed in ref. 37 and 38 to the derivation of useful formulae for the statistical properties of a system of particles enclosed in a cylinder.

The entropy of a macroscopic system confined in a cylinder of fixed radius  $R$  and length  $L \gg R$  obeys the scaling relation

$$S(\lambda E, \lambda L, A, \lambda N) = \lambda S(E, L, A, N), \quad (\text{A.1})$$

$E$  being the internal energy and  $A = 4\pi R^2$  the cross-section area. From the above equation it readily follows that

$$S(E, L, A, N) = \frac{1}{T}E + \frac{P_L A}{T}L - \frac{\mu}{T}N, \quad (\text{A.2})$$

where

$$\frac{1}{T} = \frac{\partial S}{\partial E}\bigg|_{L,A,N}, \quad \frac{P_L A}{T} = \frac{\partial S}{\partial L}\bigg|_{E,A,N}, \quad \text{and} \quad \frac{\mu}{T} = -\frac{\partial S}{\partial N}\bigg|_{E,A,L}. \quad (\text{A.3})$$

On the other hand, if we call  $P_A L/T$  the variable conjugate to  $A$ , the first law of thermodynamics prescribes that

$$dS = \frac{1}{T}dE + \frac{P_L A}{T}dL + \frac{P_A L}{T}dA - \frac{\mu}{T}dN \quad (\text{A.4})$$

with generally distinct  $P_A$  and  $P_L$  values, both approaching the bulk pressure when  $R$  is large. A comparison of eqn (A.4) with eqn (A.2) yields the Gibbs–Duhem relation:

$$Ed\frac{1}{T} + Ld\frac{P_L A}{T} - \frac{P_A L}{T}dA - Nd\frac{\mu}{T} = 0. \quad (\text{A.5})$$

The Massieu function derived from  $S$  after substituting  $E$  with  $1/T$  and  $L$  with  $P_L A/T$  is then

$$S\left[\frac{1}{T}, \frac{P_L A}{T}\right] = S - \frac{1}{T}E - \frac{P_L A}{T}L \equiv \tilde{S}, \quad (\text{A.6})$$

which is meant to be a function of  $1/T$ ,  $P_L A/T$ ,  $A$ ,  $N$  through the first two eqn (A.3). Its differential is:

$$d\tilde{S} = -Ed\frac{1}{T} - Ld\frac{P_L A}{T} + \frac{P_A L}{T}dA - \frac{\mu}{T}dN. \quad (\text{A.7})$$

In particular, the following relation holds:

$$\frac{P_A L}{T} = \frac{\partial \tilde{S}}{\partial A}\bigg|_{1/T, P_L A/T, N}, \quad (\text{A.8})$$

which turns out to be useful for calculating  $P_A$  in a simulation.

We decided to work with fixed values of  $T$ ,  $P_L$ ,  $A$ , and  $N$ , corresponding to an ensemble with mixed canonical and isothermal–isobaric features. The pertinent partition function is

$$\mathcal{A} = \frac{1}{L_0} \int_0^{L_0} dL \exp\{-\beta P_L A L\} \frac{1}{N! A^{3N}} \int_{(LA)^N} d^{3N}x \exp\{-\beta U(\mathbf{x}^N)\}, \quad (\text{A.9})$$

where  $L_0$  is an arbitrary length,  $\beta = (k_B T)^{-1}$ ,  $A$  is the thermal wavelength, and  $U$  is the potential energy (the rightmost integral in eqn (A.9) is performed over the cylinder for every particle). The fundamental prescription to derive thermodynamics from statistical mechanics is:

$$\tilde{S}(1/T, P_L A/T, A, N) = k_B \ln \mathcal{A}, \quad (\text{A.10})$$

hence the values of  $P_A$  and  $\langle L \rangle$  are in terms of the system Hamiltonian. While the calculation of  $\langle L \rangle$  in the simulation is obvious, a virial-like formula applies for  $P_A$  that is derived below. Assume  $\mathbf{x} = (\rho, \phi, z)$  to be the cylindrical coordinates of a generic particle, and let scaled (primed) coordinates be introduced in

order to eliminate  $L$  and  $A$  from the integration boundary in eqn (A.9). Their definitions are  $\rho = R\rho'$ ,  $\phi = \phi'$ ,  $z = Lz'$ , with  $R = \sqrt{A/\pi}$ . Hence,  $d^3x = \rho d\rho d\phi dz = (LA/\pi)d^3x'$  with  $d^3x' = \rho' d\rho' d\phi' dz'$ , yielding:

$$\Delta = \frac{1}{L_0} \frac{A^N}{N! A^{3N} \pi^N} \int_0^{+\infty} dL L^N \exp\{-\beta P_L A L\} \times \int_{(2\pi)^N} d^3N x' \exp\left\{-\beta \hat{U}(\mathbf{x}'^N)\right\}, \quad (\text{A.11})$$

where the last integral is over the 3D interval  $[0, 1] \times [0, 2\pi] \times [0, 1]$  for every  $\mathbf{x}'$  and

$$\hat{U}(\mathbf{x}'^N) = \sum_{i < j} u\left(\sqrt{R^2(x'_{ij}{}^2 + y'_{ij}{}^2) + L^2 z'_{ij}{}^2}\right) \quad (\text{A.12})$$

with  $x'_{ij} = \rho'_i \cos \phi'_i - \rho'_j \cos \phi'_j$ ,  $y'_{ij} = \rho'_i \sin \phi'_i - \rho'_j \sin \phi'_j$ , and  $z'_{ij} = z'_i - z'_j$ . In particular, we observe that

$$\frac{\partial \hat{U}}{\partial R} = \frac{1}{R} \sum_{i < j} u'(r_{ij}) \frac{x_{ij}{}^2 + y_{ij}{}^2}{r_{ij}} \quad \text{and} \quad \frac{\partial \hat{U}}{\partial L} = \frac{1}{L} \sum_{i < j} u'(r_{ij}) \frac{z_{ij}{}^2}{r_{ij}}, \quad (\text{A.13})$$

where the results have been expressed in terms of the original Cartesian coordinates. Upon inserting eqn (A.10) into the second of eqn (A.8), we finally get:

$$\beta P_A = \frac{N}{A \langle L \rangle} + \frac{\beta}{A \langle L \rangle} \left\langle -\frac{1}{2} \sum_{i < j} u'(r_{ij}) \frac{x_{ij}{}^2 + y_{ij}{}^2}{r_{ij}} \right\rangle, \quad (\text{A.14})$$

$\langle \dots \rangle$  being an average over the  $(\beta, \beta P_L A, A, N)$  ensemble. Eqn (A.14) is clearly reduced to the usual virial formula when both  $R$  and  $L$  are large.

We now derive a Widom-like formula for the chemical potential  $\mu$ . It follows from the very definition of  $\mu$  that

$$\beta \mu = -\frac{\partial \ln \Delta}{\partial N} \Big|_{\beta, \beta P_L A, A} \simeq -\ln \frac{\Delta_{N+1}}{\Delta_N}, \quad (\text{A.15})$$

where the second step applies for large values of  $N$ . The potential energy of a system of  $N + 1$  particles can be written as the sum of the interaction energy of the first  $N$  particles plus a residual term  $\Delta U$  involving the interaction of the  $(N + 1)$ -th particle with the others. Upon plugging eqn (A.9) in eqn (A.15), we readily obtain:

$$\beta \mu = -\ln \left( \frac{1}{(N+1)A^3} \frac{\int dL \exp\{-\beta P_L A L\} \int_{(AL)^N} d^3N x \exp\{-\beta U_N\} \int_{AL} d^3 x_{N+1} \exp\{-\beta \Delta U\}}{\int dL \exp\{-\beta P_L A L\} \int_{(AL)^N} d^3N x \exp\{-\beta U_N\}} \right), \quad (\text{A.16})$$

which can be reshuffled as

$$\beta \mu = \ln(\beta P_L A^3) - \ln \left[ \beta P_L \left\langle \frac{AL}{N+1} \times \frac{1}{AL} \int_{AL} d^3 x_{N+1} \exp\{-\beta \Delta U\} \right\rangle \right], \quad (\text{A.17})$$

the last average being taken over the  $N$ -particle system, *i.e.*, over the Boltzmann distribution of the  $(\beta, \beta P_L A, A, N)$  ensemble. The

two terms in eqn (A.17) are identified with the ideal and excess contributions, respectively, by just noticing that the first term follows through eqn (A.15) from the exact ideal partition function,

$$\Delta_{\text{id}} = \frac{1}{L_0} \int_0^{+\infty} dL \exp\{-\beta P_L A L\} \frac{(AL)^N}{N! A^{3N}} = \frac{1}{(\beta P_L A^3)^N \beta P_L A L_0}. \quad (\text{A.18})$$

Let us now explain how the Boltzmann distribution of the  $(\beta, \beta P_L A, A, N)$  ensemble is sampled in a MC simulation. A generic ensemble average reads

$$\langle \hat{\mathcal{O}} \rangle = \frac{\int dL L^N \exp\{-\beta P_L A L\} \int_{\pi^N} d^3N x' \hat{\mathcal{O}}(\mathbf{x}'^N) \exp\left\{-\beta \hat{U}(\mathbf{x}'^N)\right\}}{\int dL L^N \exp\{-\beta P_L A L\} \int_{\pi^N} d^3N x' \exp\left\{-\beta \hat{U}(\mathbf{x}'^N)\right\}} \equiv \langle \hat{\mathcal{O}} \rangle_{\pi} \quad (\text{A.19})$$

with

$$\pi(\mathbf{x}'^N) \propto \exp\{-\beta[\hat{U}(\mathbf{x}'^N) + P_L A L - k_B T N \ln L]\}. \quad (\text{A.20})$$

The  $\pi$  distribution can be sampled by means of a Metropolis algorithm with trial moves of two types: (i) a small displacement of a randomly chosen particle, and (ii) a random updating of the tube length  $L$ . In case (i), the ratio between the  $\pi$  values after and before the move is simply

$$\frac{\pi_{\text{fin}}}{\pi_{\text{in}}} = \exp\{-\beta \delta U\}, \quad (\text{A.21})$$

$\delta U$  being the difference between the final and initial values of the interaction energy pertaining to the selected particle. In case (ii), the scaled coordinates of the particles are kept fixed while the box length is incremented by  $\delta L$  (therefore, only the absolute  $z$  coordinates are affected by the move). The  $\pi$  ratio is now:

$$\frac{\pi_{\text{fin}}}{\pi_{\text{in}}} = \exp\left\{-\beta \left(\delta U + P_L A \delta L - N k_B T \ln \frac{L + \delta L}{L}\right)\right\}. \quad (\text{A.22})$$

In both cases, the acceptance probability of the move is  $\min\{1, \pi_{\text{fin}}/\pi_{\text{in}}\}$ . The maximum amplitude of the particle displacement in a type-(i) move and of  $\delta L$  in a type-(ii) move were adjusted

during the equilibration stage of the run so as to ensure a fraction of accepted moves close to 50%. These maximum amplitudes are kept fixed instead during the production stage. In a single MC cycle or sweep, only one move on average is a type-(ii) move.

Finally, we quote the formulae for the main response functions (*i.e.*, isobaric specific heat, isothermal compressibility, and isobaric expansion coefficient) in the  $(\beta, \beta P_L A, A, N)$  ensemble:

$$\begin{aligned}
C_{P_L} &= T \left. \frac{\partial S}{\partial T} \right|_{P_L} = \frac{3}{2} k_B + \frac{1}{N(k_B T)^2} \left( \langle H^2 \rangle - \langle H \rangle^2 \right) \quad \text{with} \quad \bar{H} = \frac{3}{2} N k_B T + U + P_L A L, \\
K_T &= - \left. \frac{1}{L} \frac{\partial L}{\partial P_L} \right|_T = \frac{A}{k_B T L} \left( \langle L^2 \rangle - \langle L \rangle^2 \right), \\
\alpha_{P_L} &= \left. \frac{1}{L} \frac{\partial L}{\partial T} \right|_{P_L} = \frac{1}{L k_B T^2} \left( \langle \bar{E} L \rangle - \langle \bar{E} \rangle \langle L \rangle \right) \quad \text{with} \quad \bar{E} = \frac{3}{2} N k_B T + U.
\end{aligned} \tag{A.23}$$

The derivation of these formulae is straightforward, even though rather lengthy. Considering, for example, the case of the isobaric specific heat, one first observes that

$$\left. \frac{\partial S}{\partial T} \right|_{P_L} = - \frac{1}{T^2} \frac{\partial S}{\partial (1/T)} - \frac{P_L A}{T^2} \frac{\partial S}{\partial (P_L A/T)} \tag{A.24}$$

and

$$S(1/T, P_L A/T, A, N) = \tilde{S} - \frac{1}{T} \frac{\partial \tilde{S}}{\partial (1/T)} - \frac{P_L A}{T} \frac{\partial \tilde{S}}{\partial (P_L A/T)}. \tag{A.25}$$

Putting eqn (A.24) and (A.25) together, we find:

$$\begin{aligned}
C_{P_L} &= \frac{1}{T^2} \frac{\partial^2 \tilde{S}}{\partial (1/T)^2} + \frac{2 P_L A}{T^2} \frac{\partial^2 \tilde{S}}{\partial (1/T) \partial (P_L A/T)} \\
&\quad + \frac{(P_L A)^2}{T^2} \frac{\partial^2 \tilde{S}}{\partial (P_L A/T)^2}.
\end{aligned} \tag{A.26}$$

Other useful relations are

$$\begin{aligned}
k_B \frac{\partial^2 \tilde{S}}{\partial (1/T)^2} &= \langle H^2 \rangle - \langle H \rangle^2, \\
k_B \frac{\partial^2 \tilde{S}}{\partial (1/T) \partial (P_L A/T)} &= \langle H L \rangle - \langle H \rangle \langle L \rangle, \\
k_B \frac{\partial^2 \tilde{S}}{\partial (P_L A/T)^2} &= \langle L^2 \rangle - \langle L \rangle^2,
\end{aligned} \tag{A.27}$$

with  $H = K + U + P_L A L$  ( $K$  is the kinetic energy and  $H$  a sort of enthalpy), which follow from eqn (A.9) and (A.10). Upon inserting eqn (A.27) into eqn (A.26), the first equation of eqn (A.23) eventually follows.

## Acknowledgements

A. S. is grateful to the National Research Foundation of South Africa for funding his sabbatical stay at the Dipartimento di Fisica e di Scienze della Terra of the University of Messina.

## References

- 1 R. O. Erikson, *Science*, 1973, **181**, 705.
- 2 M. C. Gordillo, B. Martínez-Haya and J. M. Romero-Enrique, *J. Chem. Phys.*, 2006, **125**, 144702.
- 3 F. J. Durán-Olivencia and M. C. Gordillo, *Phys. Rev. E: Stat., Nonlinear, Soft Matter Phys.*, 2009, **79**, 061111.
- 4 H. C. Huang, S. K. Kwak and J. K. Singh, *J. Chem. Phys.*, 2009, **130**, 164511.
- 5 H.-K. Chan, *Phys. Rev. E: Stat., Nonlinear, Soft Matter Phys.*, 2011, **84**, 050302(R).
- 6 A. Mughal, H. K. Chan, D. Weaire and S. Hutzler, *Phys. Rev. E: Stat., Nonlinear, Soft Matter Phys.*, 2012, **85**, 051305.
- 7 M. W. Maddox and K. E. Gubbins, *J. Chem. Phys.*, 1997, **107**, 9659.
- 8 M. A. Lohr, A. M. Alsayed, B. G. Chen, Z. Zhang, R. D. Kamien and A. G. Yodh, *Phys. Rev. E: Stat., Nonlinear, Soft Matter Phys.*, 2010, **81**, 040401(R).
- 9 D. Liu, Y. Zhang, C.-C. Chen, C.-Y. Mou, P. H. Poole and S.-H. Chen, *Proc. Natl. Acad. Sci. U. S. A.*, 2007, **104**, 9570.
- 10 F. Mallamace, C. Branca, M. Broccio, C. Corsaro, C.-Y. Mou and S.-H. Chen, *Proc. Natl. Acad. Sci. U. S. A.*, 2007, **104**, 18387.
- 11 R. Mancinelli, F. Bruni and M. A. Ricci, *J. Phys. Chem. Lett.*, 2010, **1**, 1277.
- 12 E. B. Moore, E. de la Llave, K. Welke, D. A. Scherlis and V. Molinero, *Phys. Chem. Chem. Phys.*, 2010, **12**, 4124.
- 13 A. A. Milischuk and B. M. Ladanyi, *J. Chem. Phys.*, 2011, **135**, 174709.
- 14 A. K. Soper, *J. Phys.: Condens. Matter*, 2012, **24**, 064107.
- 15 D. T. Limmer and D. Chandler, *J. Chem. Phys.*, 2012, **137**, 044509.
- 16 M. Erko, D. Wallacher, A. Hoell, T. Hauss, I. Zizak and O. Paris, *Phys. Chem. Chem. Phys.*, 2012, **14**, 3852.
- 17 F. G. Alabarse, J. Haines, O. Cambon, C. Levelut, D. Bourgogne, A. Haidoux, D. Granier and B. Coasne, *Phys. Rev. Lett.*, 2012, **109**, 035701.
- 18 F. H. Stillinger, *J. Chem. Phys.*, 1976, **65**, 3968.
- 19 A. Lang, C. N. Likos, M. Watzlawek and H. Löwen, *J. Phys.: Condens. Matter*, 2000, **12**, 5087.
- 20 S. Prestipino, F. Saija and P. V. Giaquinta, *Phys. Rev. E: Stat., Nonlinear, Soft Matter Phys.*, 2005, **71**, 050102(R).
- 21 C. Speranza, S. Prestipino and P. V. Giaquinta, *Mol. Phys.*, 2011, **109**, 3001.
- 22 S. Prestipino, C. Speranza and P. V. Giaquinta, *Soft Matter*, 2012, **8**, 11708.
- 23 Z. Yan, S. V. Buldyrev, N. Giovanbattista and H. E. Stanley, *Phys. Rev. Lett.*, 2005, **95**, 130604.
- 24 E. A. Jagla, *J. Chem. Phys.*, 1999, **111**, 8980.
- 25 A. B. de Oliveira, P. A. Netz, T. Colla and M. C. Barbosa, *J. Chem. Phys.*, 2006, **125**, 124503.
- 26 J. R. Errington, T. M. Truskett and J. Mittal, *J. Chem. Phys.*, 2006, **125**, 244502.

- 27 W. P. Krekelberg, T. Kumar, J. Mittal, J. R. Errington and T. M. Truskett, *Phys. Rev. E: Stat., Nonlinear, Soft Matter Phys.*, 2009, **79**, 031203.
- 28 S. Prestipino, F. Saija and G. Malescio, *J. Chem. Phys.*, 2010, **133**, 144504.
- 29 G. Malescio, S. Prestipino and F. Saija, *Mol. Phys.*, 2011, **109**, 2837.
- 30 S. Prestipino, F. Saija and P. V. Giaquinta, *J. Chem. Phys.*, 2012, **137**, 104503.
- 31 T. M. Truskett, P. G. Debenedetti and S. Torquato, *J. Chem. Phys.*, 2001, **114**, 2401.
- 32 C. N. Likos, *Phys. Rep.*, 2001, **348**, 267.
- 33 S. Prestipino, F. Saija and P. V. Giaquinta, *Phys. Rev. Lett.*, 2011, **106**, 235701.
- 34 S. Prestipino, F. Saija and P. V. Giaquinta, *J. Chem. Phys.*, 2005, **123**, 144110.
- 35 P. R. ten Wolde, M. J. Ruiz-Montero and D. Frenkel, *J. Chem. Phys.*, 1996, **104**, 9932.
- 36 H. Kanno, R. J. Speedy and C. A. Angell, *Science*, 1975, **189**, 880.
- 37 R. Evans and U. Marini Bettolo Marconi, *J. Chem. Phys.*, 1987, **86**, 7138.
- 38 D. J. Diestler, M. Schoen, J. E. Curry and J. H. Cushman, *J. Chem. Phys.*, 1994, **100**, 9140.
- 39 Y. Kondo and K. Takayanagi, *Science*, 2000, **289**, 606.
- 40 E. Tosatti and S. Prestipino, *Science*, 2000, **289**, 561.
- 41 E. Tosatti, S. Prestipino, S. Kostlmeier, A. Dal Corso and F. D. Di Tolla, *Science*, 2001, **291**, 288.
- 42 S. Prestipino, F. Saija and G. Malescio, *Soft Matter*, 2009, **5**, 2795.
- 43 See, e.g., P. Mausbach and H.-O. May, *Fluid Phase Equilib.*, 2006, **249**, 17.